

1 **Improved Estimation of Glacial-Earthquake Size**
2 **Through New Modeling of the Seismic Source**

3 **Kira G. Olsen¹, Meredith Nettles¹, L. Mac Cathles², Justin C. Burton³, Tavi**
4 **Murray⁴, Timothy D. James⁵**

5 ¹Lamont-Doherty Earth Observatory, Columbia University, New York, NY 10964, USA

6 ²Climate and Space Sciences and Engineering, University of Michigan, Ann Arbor, MI 48109, USA

7 ³Department of Physics, Emory University, Atlanta, GA 30322, USA

8 ⁴Glaciology Group, Department of Geography, College of Science, Swansea University, Swansea SA2 8PP,
9 UK

10 ⁵Dept of Geography and Planning, Queen's University, Kingston, Ontario, Canada K7L 3N6

Corresponding author: Meredith Nettles, nettles@ldeo.columbia.edu

This is the author manuscript accepted for publication and has undergone full peer review but has not been through the copyediting, typesetting, pagination and proofreading process, which may lead to differences between this version and the [Version of Record](#). Please cite this article as [doi: 10.1029/2021JF006384](https://doi.org/10.1029/2021JF006384).

This article is protected by copyright. All rights reserved.

11
12
13
14
15
16
17

Key Points:

- A physics-based source model for glacial-earthquake modeling improves recovery of seismic-magnitude values
- Maximum force is less sensitive to model choices than M_{CSF} and is preferred for describing glacial-earthquake size
- A rapid force reversal during iceberg calving is the most important feature to capture in a glacial-earthquake source model

Abstract

The number of gigaton-sized iceberg-calving events occurring annually at Greenland glaciers is increasing, part of a larger trend of accelerating mass loss from the Greenland Ice Sheet.

Though visual observation of large calving events is rare, ~ 60 glacial earthquakes generated by these calving events are currently recorded each year by regional and global seismic stations. An empirical relationship between iceberg size and M_{CSF} , a summary measure of glacial-earthquake size, was recently demonstrated by Olsen and Nettles (2019).

However, M_{CSF} is known to be sensitive to choices made in modeling the seismic source.

We incorporate constraints on the seismic source from laboratory studies of calving and test multiple source time functions using synthetic and observed glacial-earthquake waveforms. We find that a simple, fixed time function with a shape informed by laboratory results greatly improves estimates of earthquake size. The average ratio of estimated to true peak force values is 1.03 for experiments using our preferred source model, compared with an average of 0.3 for models used in previous studies. We find that maximum-force values estimated from waveform modeling depend far less on model choices than does M_{CSF} , and therefore prefer maximum force as a measure of glacial-earthquake size. Using both synthetic and real data, we confirm a correlation between maximum force and iceberg mass. Our results support the possibility of developing useful scaling relationships between seismic observables and physical parameters controlling glacier calving.

Plain Language Summary

The Greenland Ice Sheet is losing ice mass. About half of that ice is lost when large icebergs break off, or calve, from the fronts of glaciers into the ocean. Knowing the sizes of these icebergs would be valuable, but iceberg calving is rarely captured on camera. However, the largest icebergs produce seismic signals when they calve, referred to as glacial earthquakes. We investigate the relationship between the size of an iceberg and the magnitude of the glacial earthquake it produces, building new models to describe the forces that generate a glacial earthquake. Previously, most details of the force evolution during iceberg calving were unknown. We use observations from laboratory experiments conducted using a plastic block in a tank of water, built to mimic the glacier-ocean setting. We find that incorporating information from these laboratory experiments into our seismic model greatly improves estimates of earthquake size. Using our new models, we confirm a correlation between glacial-earthquake magnitude and iceberg size, and show that our improved estimates are likely to be more realistic. Our results suggest that using seismic information to estimate iceberg size and related quantities is a promising path forward.

1 Introduction

Ice loss from the Greenland Ice Sheet has accelerated in recent years, and up to half of that mass loss results from iceberg calving (Enderlin et al., 2014). More than 200 large glaciers around Greenland advect ice from the interior of the ice sheet to the ocean (Moon et al., 2012), and during the summer months, multiple large iceberg-calving events can

58 occur at a single glacier over the course of a day (e.g., Olsen & Nettles, 2019). Some of
59 the largest calving events involve icebergs of $\sim 1 \text{ km}^3$ that are driven to capsize against
60 the glacier terminus by buoyancy forces. These rotational calving events generate glacial
61 earthquakes (Ekström et al., 2003), magnitude ~ 5 seismic events that can be detected
62 using the broadband stations of the Global Seismographic Network (GSN) and the Green-
63 land Ice Sheet Monitoring Network (GLISN). During calving, the motion of the iceberg
64 and the water it displaces exert a time-varying force on the Earth. The seismic waves
65 generated by these forces contain information about the physics of the calving process,
66 and about the iceberg that calved.

67 Glacial earthquakes are generated by a style of mass loss known as buoyancy-driven
68 calving, which, at tidewater glaciers, occurs when a glacier terminates close to its ground-
69 ing line. If the glacier terminus is driven below isostatic equilibrium as it flows into the
70 water, buoyancy forces will push upward on the short floating ice tongue, driving basal
71 crevassing and subsequent iceberg calving (James et al., 2014; Murray, Selmes, et al., 2015).
72 Icebergs lost through buoyancy-driven calving may extend the full glacier thickness (up
73 to $\sim 1 \text{ km}$) and have been observed to have aspect ratios of $\sim 0.1\text{-}0.5$, where the short di-
74 mension is measured along flow (Amundson et al., 2010; James et al., 2014; Murray, Net-
75 tles, et al., 2015; Olsen & Nettles, 2019; Walter et al., 2012). This tall, narrow geome-
76 try is unstable and leads the iceberg to capsize against the terminus (Figure 1). The ma-
77 jority of these calving events involve bottom-out iceberg rotation, where the top of the
78 iceberg remains pinned against the terminus during the first stages of rotation while the
79 lower portion of the iceberg rotates up in the water column and away from the termi-

80 nus. A limited number of top-out calving events have also been observed (e.g., Walter
81 et al., 2012), but this calving geometry is rare.

82 During iceberg capsize, time-varying horizontal and vertical forces are applied to
83 the Earth and generate the seismic waves recorded as a glacial earthquake. The largest-
84 amplitude force, horizontal and oriented perpendicular to the calving face, is generated
85 by the iceberg accelerating into the fjord and away from the glacier terminus during cap-
86 size (Figure 1; Nettles & Ekström, 2010; Murray, Nettles, et al., 2015). A small verti-
87 cal force is simultaneously generated behind the rotating iceberg by a pressure drop in
88 the water column (Murray, Nettles, et al., 2015). The sum of these forces is a subhor-
89 izontal force acting at the glacier terminus. The orientation and magnitude of the force,
90 along with estimates of event location and timing, can be obtained by analysis of the seis-
91 mic waves produced.

92 Systematic analysis of glacial-earthquake seismic data (Olsen & Nettles, 2017; Tsai
93 & Ekström, 2007; Veitch & Nettles, 2012) has led to a catalog of glacial earthquakes that
94 now spans more than two decades and forms a robust seismic record of iceberg calving
95 including nearly 450 glacial earthquakes. The rate of earthquake occurrence has increased
96 with time (e.g., Ekström et al., 2006; Olsen & Nettles, 2017); currently, ~60 glacial earth-
97 quakes occur in Greenland each year. Study of glacial earthquakes has advanced our un-
98 derstanding of numerous aspects of mass loss around Greenland, including the spatial
99 evolution of buoyancy-driven calving (Nettles & Ekström, 2010; Olsen & Nettles, 2017;
100 Veitch & Nettles, 2012), seasonal patterns in calving (Ekström et al., 2006; Olsen & Net-
101 tles, 2017; Veitch & Nettles, 2012), and evolution of terminus dynamics at individual glaciers

102 (Murray, Selmes, et al., 2015; Olsen & Nettles, 2017, 2019; Veitch & Nettles, 2012; Wal-
103 ter et al., 2012).

104 An ongoing goal of glacial-earthquake analysis has been to relate the seismic mag-
105 nitude of a glacial earthquake to the size of a calving iceberg. Clarifying such a relation-
106 ship would allow permanent seismic stations to be used for remote quantification of mass
107 loss through calving at numerous glaciers in Greenland in near-real time. In a recent study
108 (Olsen & Nettles, 2019), we used iceberg-size estimates from twelve calving events to pub-
109 lish the first empirical demonstration of a correlation between iceberg size and a mea-
110 sure of glacial-earthquake magnitude, M_{CSF} , obtained using centroid-single-force (CSF)
111 analysis of the seismic waveforms. We have subsequently analyzed nine additional calv-
112 ing events, and find results in close agreement with the previously reported trend (Fig-
113 ure 2). The relationship between M_{CSF} and iceberg size that we observe follows the trend
114 predicted by a very simple geometric model relating the seismic magnitude of a grav-
115 itationally driven seismic event to the mass of the accelerating object multiplied by the
116 distance over which it accelerates (Kawakatsu, 1989). For a glacial earthquake, the min-
117 imum value for M_{CSF} corresponds to the iceberg mass multiplied by the distance required
118 for the iceberg to capsize (see Figure 1). However, the seismically determined M_{CSF} val-
119 ues are approximately an order of magnitude smaller than predicted by this simple, ge-
120 ometric model, given the observed dimensions of each iceberg (Figure 2). The empiri-
121 cal demonstration of a clear relationship between seismic magnitude and iceberg size,
122 combined with the observed relationship with the simple model, suggests that a more
123 detailed investigation is merited.

124 The assumption most likely to affect seismically derived estimates of M_{CSF} is that
125 of the time history of the applied force, or force-time function, specified in waveform mod-
126 eling. M_{CSF} values have long been known to be sensitive to the duration of the force-
127 time function (i.e., the seismic source model) used in analysis. Tsai et al. (2008) consid-
128 ered a range of force-time functions and found that glacial-earthquake waveforms could
129 be modeled well using a 50-s, symmetric, double “boxcar” force model, or asymmetric
130 boxcar models of varying durations. Veitch and Nettles (2012) demonstrated that retain-
131 ing the boxcar shape but varying the duration of the force function by 20% changed the
132 estimated M_{CSF} value by 20-30%. Extending this analysis, we find that doubling the
133 source-model duration can increase the estimated M_{CSF} value by a factor of 4 or more,
134 though estimates of force geometry change very little. Because the true duration and char-
135 acter of the seismic source is not known for individual calving events, all glacial earth-
136 quakes in the published catalog (Olsen & Nettles, 2017, 2019; Tsai & Ekström, 2007; Veitch
137 & Nettles, 2012) have been analyzed using the same, fixed model as an approximation
138 of the seismic source.

139 Ideally, the seismic analysis could be made insensitive to the duration and shape
140 of the force-time history; or, a description of the force-time history could be extracted
141 directly from the waveforms. However, glacial-earthquake signals are dominated by en-
142 ergy within a narrow frequency band, restricting such approaches. Centroid-single-force
143 (CSF) analysis of glacial earthquakes (e.g., Ekström et al., 2003) is typically conducted
144 using surface waves recorded in the period band 50–150 s, the same period band used
145 in centroid-moment-tensor (CMT) analysis of tectonic earthquakes of similar size (e.g.,

146 Ekström et al., 2012). In this band, signal strength is high, Earth noise is relatively low,
147 and the Earth's lateral velocity heterogeneity is well described. Because tectonic earth-
148 quakes of this size have durations of only a few seconds, much shorter than the period
149 of the waves analyzed, estimates of earthquake size are only weakly sensitive to the choice
150 of source time function. In contrast, the long durations of glacial earthquakes (at least
151 several 10s of seconds) are similar to the period of the waves analyzed, making estimates
152 of earthquake size more strongly sensitive to the choice of source time function. At pe-
153 riods longer than the glacial-earthquake duration, seismic-wave amplitudes are very small,
154 owing to the small sizes of even the largest glacial earthquakes ($M \sim 5$), such that, even
155 at quiet, nearby seismic stations, glacial-earthquake energy is below noise levels at pe-
156 riods longer than 100–150 s. Further, while the robust high-frequency energy generated
157 by most tectonic earthquakes can allow reconstruction of the source time function di-
158 rectly from recorded seismic waves, the slow source of glacial earthquakes (iceberg ro-
159 tation over 10s to 100s of seconds) results in seismic waves that are severely depleted in
160 high-frequency energy at periods shorter than ~ 30 –50 s. This high-frequency depletion
161 for glacial-earthquake events has long been recognized (Ekström et al., 2003), and is the
162 reason glacial earthquakes go undetected by short-period body-wave detection algorithms;
163 Olsen and Nettles (2019) recently confirmed that glacial earthquakes lack coherent sig-
164 nal at short periods even at GLISN seismometers located within 100 km of glacier ter-
165 mini.

166 In this study, we explore an approach in which we incorporate information from
167 non-seismic data to elucidate the character of the force-time history of a calving iceberg

168 that generates a glacial earthquake. Analog experiments of iceberg calving in the lab-
169 oratory have proven valuable in advancing understanding of buoyancy-driven calving (Cathles
170 et al., 2015; Murray, Nettles, et al., 2015). In laboratory experiments conducted by Cathles
171 et al. (2015), iceberg calving is simulated by capsizing of a plastic block within a water-
172 filled tank (Figure 3). Sensors located within the ‘glacier’ terminus record force and pres-
173 sure timeseries throughout the capsizing of the analog iceberg, thereby providing obser-
174 vations of the time-varying horizontal and vertical forces applied by a calving iceberg
175 to the solid Earth, in a laboratory setting. When scaled up to glacier dimensions, the
176 force histories recorded in laboratory experiments closely match the duration and char-
177 acter of GPS-derived observations of glacier displacement during calving (Murray, Net-
178 tles, et al., 2015). The recorded force histories are also similar to force histories calcu-
179 lated in numerical simulations (Sergeant et al., 2018). The consistency between the force
180 histories observed in laboratory experiments, GPS observations, and numerical-modeling
181 results suggests that the laboratory experiments, while not real Earth observations, likely
182 capture the critical aspects of the force history at the glacier front during generation of
183 a glacial earthquake. In addition, seismic-magnitude values, M_{CSF} , calculated for the
184 tank events using the same seismic modeling approach and 50-s boxcar source model used
185 in standard analysis of glacial earthquakes are in close agreement with results for real
186 glacial earthquakes (Figure 2).

187 We employ an existing set of laboratory experiments of iceberg calving (Burton et
188 al., 2012; Cathles et al., 2015) to construct new models of the seismic source time func-
189 tion for use in glacial-earthquake waveform modeling. This is the first introduction of

190 such constraints into seismic modeling of glacial earthquakes. We assess the ability of
 191 source models of this type to return improved estimates of source parameters, using both
 192 seismograms from synthetic events and observed glacial earthquakes. We explore the re-
 193 lationship between iceberg size and seismic magnitude, and consider additional metrics
 194 of seismic magnitude beyond M_{CSF} , including peak force and peak momentum. By in-
 195 corporating laboratory-based constraints into seismic analysis, we demonstrate the util-
 196 ity of a more sophisticated, physics-based source model for glacial earthquakes, and lay
 197 out a framework for future work to further advance glacial-earthquake modeling.

198 2 Background

199 2.1 Estimation of the Seismic Source

200 The time-varying force exerted by a calving iceberg in the direction opposite its
 201 acceleration is similar in geometry to that generated by a landslide mass accelerating down-
 202 hill. Glacial earthquakes, like landslides, can be modeled using a centroid-single-force
 203 (CSF) approach (Ekström et al., 2003; Kawakatsu, 1989). The CSF technique is closely
 204 related to the CMT technique (e.g., Dziewonski et al., 1981) used to model the sources
 205 of tectonic earthquakes. Ground motion recorded at a seismic station depends on the
 206 source that generates the waves and on the Earth structure through which the waves travel.
 207 Ground motion u in direction k recorded at a seismic station at location \mathbf{r} can be writ-
 208 ten

$$u_k(\mathbf{r}, t) = \sum_{i=1}^N \Psi_{ik}(\mathbf{r}, \mathbf{r}_s, t) * S_i(t) \cdot f_i \quad (1)$$

209 where the $*$ denotes convolution, and the Green function Ψ describes the predicted
210 seismogram generated by a point force \mathbf{f} , acting at location \mathbf{r}_s , for a given model for Earth
211 structure. In the CMT approach, the vector f_i contains the amplitudes of the six
212 independent elements of the moment-rate tensor, and $N = 6$. In CSF analysis f_i contains
213 the amplitude of a point force acting in direction i , and $N = 3$, with the summation over
214 the three orthogonal components of the force vector (South, East, and up). The time
215 history of the seismic source is represented by the source time function $S_i(t)$. In most
216 CMT and CSF applications, $S_i(t) = S(t)$, for all i , such that the shape of the time
217 function is the same for each component of the moment tensor or force vector.

218 The formulation of the ground-motion equation is thus similar for CMT and CSF
219 analysis, and accurate ground-motion prediction relies upon both a robust model of Earth
220 structure and a model of the source time function. A point-source approximation in space
221 is adequate for long-period data where the wavelength is much greater than the spatial
222 extent of the source. This condition is met both for glacial earthquakes and for moderate-
223 sized tectonic earthquakes in the 50–150 s period band typically used (Ekström et al.,
224 2012) in analysis of events of this size. However, the function $S(t)$ is prescribed in both
225 CMT and CSF analysis because, in both cases, these data have insufficient sensitivity
226 to the shape of the source time function to allow its independent retrieval.

227 With models for both structure and source defined, the inverse problem can be solved
228 for f_i . In practice, the source time and location are not precisely known upon event de-
229 tection. Therefore, inversion for the elements of the source, f_i , the event time, and lo-
230 cation is conducted simultaneously, using a linearized approach (e.g., Dziewonski et al.,

231 1981; Ekström et al., 2012). In our work, we follow the implementation of Ekström et
232 al. (2012).

233 For tectonic earthquakes, the source variation with time is described by the moment-
234 rate function. In CSF analysis, the force history or its integral is used as the source time
235 function, $S(t)$. A simple, double-boxcar force model of the seismic source of glacial earth-
236 quakes (Figure 4a) has been used in analysis of all events in the glacial-earthquake cat-
237 alog to date (Olsen & Nettles, 2017, 2019; Tsai & Ekström, 2007; Veitch & Nettles, 2012).
238 This model specifies a 50-s-long, anti-symmetric source time function that represents a
239 constant force applied to the Earth for 25 s as the iceberg accelerates away from the glacier
240 terminus, followed by a 25-s constant force of equal amplitude and opposite sign as the
241 iceberg decelerates (Figure 4a).

242 The boxcar model satisfies the requirement that momentum be conserved, and has
243 been found to produce good fits to available data. Given a constant mass, the first in-
244 tegral of the CSF force history with respect to time represents the momentum history
245 of the moving mass, also known as the impulse (Figure 4b), and the twice-integrated force
246 history can be interpreted as the product of the mass and the distance over which ac-
247 celeration occurs. The value to which the mass–distance product converges (the zero-
248 frequency value) has been termed the centroid-single-force magnitude, M_{CSF} (Figure
249 4c). The M_{CSF} value is analogous to the seismic moment for a tectonic earthquake, in
250 the sense that it is a summary measure of earthquake size obtained when the event has
251 terminated. As with tectonic-earthquake studies, zero-frequency data are not necessary
252 to retrieve an estimate of this ‘zero-frequency’ value for glacial earthquakes. Instead, in

253 both tectonic- and glacial-earthquake studies, an accurate model of the seismic source
254 allows for accurate retrieval of event size.

255 **2.2 Constraints on the Shape of the Glacial-Earthquake Force History**

256 *2.2.1 Analog Laboratory Experiments and GPS Observations of Iceberg*

257 *Calving*

258 Though field observations of buoyancy-driven calving are sparse, insight has been
259 gained through analog studies simulating iceberg calving with a plastic block in a water-
260 filled tank (Figure 3; Burton et al., 2012; Amundson et al., 2012; Cathles et al., 2015).

261 During capsizing of an analog iceberg, sensors located within the tank wall record time se-
262 ries describing either the force or the pressure changes generated by iceberg rotation and
263 hydrodynamic effects (Figure 5; Cathles et al., 2015). High-rate photographic imagery
264 allows synchronization in time of the force and pressure records for a given iceberg. Ad-
265 ditional details of the laboratory setup are given by Burton et al. (2012) and Murray,
266 Nettles, et al. (2015).

267 Force and pressure histories recorded in the lab can be scaled up to glacier dimen-
268 sions when the ratio between iceberg height in the field and in the laboratory is known
269 (Amundson et al., 2012; Burton et al., 2012; MacAyeal et al., 2011). Scaled-up labora-
270 tory force and pressure records predict well the glacier deflection that is observed to oc-
271 cur during iceberg calving (Murray, Nettles, et al., 2015). Furthermore, M_{CSF} values
272 calculated from synthetic seismograms generated from these scaled-up laboratory force
273 records are in close agreement with M_{CSF} values estimated for true glacial earthquakes

274 (Figure 2). The experimental data thus appear to provide a robust analog with which
275 to investigate details of the time-varying force generated during iceberg capsize, as well
276 as the relationship between iceberg size and force magnitude.

277 In this study, we focus on bottom-out buoyancy-driven calving, for which capsize
278 occurs spontaneously when a tall, narrow plastic iceberg is placed vertically within the
279 water column against one end of the tank (Figure 3). Force and pressure histories recorded
280 for analog icebergs of four different aspect ratios (Cathles et al., 2015) and scaled up to
281 a variety of iceberg heights observed in the field (Murray, Nettles, et al., 2015) are shown
282 in Figure 5. The first ~ 600 s of each horizontal-force history recorded during tank ex-
283 periments shows a gradual increase in up-glacier force amplitude, which we define as a
284 positive force, followed by a more rapid decrease (Figure 5). This part of the force his-
285 tory, during which the horizontal-force values are positive (grey-shaded portions of pan-
286 els in Figure 5), is interpreted as the glacier response to seaward iceberg acceleration dur-
287 ing capsize (Murray, Nettles, et al., 2015). The maximum up-glacier force is labeled ‘a’
288 in the upper-left panel of Figure 5. Following this acceleration phase of the force history,
289 each of the laboratory-derived horizontal-force histories contains a rapid force reversal
290 to a down-glacier (negative) force lasting approximately 20 s (‘b’ in the upper left panel
291 of Figure 5). We interpret this part of the force history as the glacier’s response to rapid
292 iceberg deceleration. The deceleration likely results from the combination of a reduced
293 buoyancy force, as the iceberg nears horizontal and no longer has significant mass out
294 of isostatic equilibrium in the water column, and the resisting force generated by water
295 in the fjord slowing the iceberg’s forward motion. A second up-glacier force peak (‘c’ in

296 the upper left panel of Figure 5) is observed following the force reversal. This up-glacier
297 force is ~ 10 -s long and reaches between $\sim 30\%$ and 100% of the amplitude of the ear-
298 lier up-glacier force ('a'). Based on videos from the tank experiments (Burton et al., 2012;
299 Cathles et al., 2015), this part of the force history appears to be generated by the ice-
300 berg rotating past horizontal so that part of the face of the iceberg that previously formed
301 the iceberg's top surface comes in contact with the glacier's calving face (see fourth panel,
302 at +8 s, in Figure 3). Such over rotation is also observed in some high-frame-rate im-
303 ages of buoyancy driven calving in the field (e.g., James et al., 2014).

304 The pressure records are out of phase with the horizontal forces during the first ~ 600 s
305 of the tank time series (grey-shaded portions of panels in Figure 5), showing a pressure
306 decrease as the horizontal up-glacier force increases. A pressure decrease in the water
307 column results in a vertical force on the solid Earth, oriented upwards. During this ac-
308 celeration phase of the force history, the up-glacier horizontal force and negative pres-
309 sure values result in an up-glacier, upward force. After the horizontal force crosses zero,
310 the pressure records become generally in phase with the horizontal force (white portion
311 of panels in Figure 5). At the time of the largest down-glacier horizontal force ('b'), pres-
312 sure deviations are near zero. During up-glacier force peak 'c', pressure excursions are
313 positive, resulting in a total force oriented downward and up glacier. The remainder of
314 the horizontal force and pressure time series for a given tank experiment are in phase,
315 and are not coherent between experiments. This final part of the time series is attributed
316 to water waves oscillating in the experimental tank (Burton et al., 2012; Cathles et al.,

317 2015). In the experimental set-up, measures are taken to damp seiche modes following
318 iceberg capsize (e.g., Murray, Nettles, et al., 2015), but waves are not fully eliminated.

319 The geometry of forces from the laboratory experiments – dominated by an up-glacier,
320 upward force reversing to an initially down-glacier, downward force – is consistent with
321 that estimated for the majority of the 450 glacial earthquakes that have been analyzed,
322 and which occurred at 15 glaciers around Greenland over the last three decades. This
323 consistency, and an initial seismic analysis of scaled-up tank data conducted by previ-
324 ous authors (Murray, Nettles, et al., 2015), suggest that the laboratory data accurately
325 represent the forces that generate the seismic signal.

326 On-glacier GPS data recorded during calving (Murray, Nettles, et al., 2015) have
327 similar characteristics to the force histories seen in all bottom-out laboratory experiments.
328 GPS instruments deployed on Helheim Glacier in East Greenland captured glacier mo-
329 tion during multiple bottom-out buoyancy-driven calving events in 2013 (Murray, Net-
330 tles, et al., 2015). During each calving event, instruments located on ice within ~ 1 km
331 of the terminus recorded the front of the glacier being displaced ~ 10 cm up-glacier for
332 ~ 300 s during the first stages of iceberg calving (Murray, Nettles, et al., 2015). The di-
333 rection of horizontal-displacement data then reverses as the glacier front moves through
334 and forward of its pre-calving position before returning to equilibrium. The shape and
335 timing of these displacement records are in close agreement with the upscaled horizontal-
336 force records from the laboratory experiments (Murray, Nettles, et al., 2015). The vertical-
337 component GPS observations show the glacier terminus drawn down and then uplifted,
338 again with the shape and timing of the records in agreement with the pressure drop and

339 increase recorded in the laboratory experiments (Murray, Nettles, et al., 2015). In glacier
340 fjords, ice mélange serves to partially damp water waves (e.g., Amundson et al., 2010),
341 and oscillations like those following peak ‘c’ (Figure 5) are not observed in glacier GPS
342 data (Murray, Nettles, et al., 2015).

343 In the following text, we refer to the first ~ 600 s of the source as the left-hand side,
344 from first signal onset to the time of the first zero crossing of the horizontal force (grey-
345 shaded portions of panels in Figure 5). We refer to the time period beginning at the first
346 force zero crossing and including the ~ 20 s down-glacier force as well as the lower-amplitude
347 up-glacier force that follows as the right-hand side of the source (white portions of pan-
348 els in Figure 5). All figures begin at -500 s, rather than -600 s, for ease of viewing.

349 *2.2.2 Numerical-Modeling Results*

350 Numerical simulations of the forces generated by buoyancy-driven iceberg capsize
351 against a glacier terminus show key characteristics of both the laboratory and field ob-
352 servations. Using a 2D finite-element approach, Sergeant et al. (2018) modeled the hor-
353 izontal contact force between an iceberg and a glacier terminus, including an approxi-
354 mation of hydrodynamic drag forces acting on the glacier-terminus system. Sergeant et
355 al. (2018) calculated the horizontal force generated during the iceberg-acceleration phase
356 of calving, from the time an iceberg begins rotation through the time the iceberg loses
357 contact with the calving face (i.e., the part of the force histories shaded grey in Figure
358 5), and predicted rotation durations of 100–200 s for icebergs with geometries like those

359 considered in this study. The shapes of the predicted force time series are similar to those
360 observed in the laboratory and inferred from GPS data.

361 With increasing aspect ratio, the force histories calculated by Sergeant et al. (2018)
362 display a steeper slope as they approach peak force, an effect also seen in laboratory re-
363 sults (Figure 5). Because the model of Sergeant et al. (2018) describes force values only
364 during the time the iceberg is in contact with the terminus, it does not capture the iceberg-
365 deceleration phase of the source that is recorded in laboratory and field observations (e.g.,
366 ‘b’ in Figure 5). It therefore does not predict any down-glacier force. However, the agree-
367 ment of the numerical-model results with the tank experiments and GPS observations
368 supports the reliability of the laboratory results, and the possibility of using this infor-
369 mation for better-informed inverse modeling of recorded seismic data.

370 *2.2.3 Limitations in Knowledge*

371 The laboratory experiments, GPS observations, and numerical-modeling results pro-
372 vide a far more detailed picture of the time history of forces acting on the solid Earth
373 during calving than was available previously. However, some important limitations re-
374 main. The available laboratory experiments measure force and pressure on the wall of
375 the experimental tank that represents the calving face (Figure 3), but not on the rest
376 of the system, including the fjord floor and walls. GPS observations are limited to the
377 glacier surface, and internal deformation must be inferred. The numerical experiments
378 provide a force history only through the time of loss of iceberg contact with the calv-

379 ing face and so do not describe forces active during the full rotation of the iceberg or dur-
380 ing its subsequent motion away from the terminus.

381 Details of the force history after the time of force reversal (i.e., during the white-
382 shaded, ‘right-hand’ side of the force histories shown in Figure 5) are particularly poorly
383 constrained. Glacier displacement records from on-ice GPS instruments (Murray, Net-
384 tles, et al., 2015) become more difficult to interpret after the rapid force reversal, in part
385 due to glacier acceleration immediately following buoyancy-driven calving (Nettles et al.,
386 2008). Laboratory records become less coherent after the iceberg first reaches horizon-
387 tal because of water waves in the tank. Available numerical models do not describe this
388 time period. None of the records demonstrate, on their own, conservation of momentum.
389 It is likely that momentum is transferred to the tsunami that propagates away from the
390 calving front following glacial earthquakes. However, only a few studies (e.g., Heller et
391 al., 2019; MacAyeal et al., 2011) have addressed the characteristics of iceberg-related tsunami-
392 genesis, and investigation of that phenomenon is beyond the scope of the current study.

393 Despite these limitations, the detail captured in the laboratory results and supported
394 by GPS data and numerical models suggests the potential for great improvement com-
395 pared with the boxcar model (Figure 4a) used previously. We therefore proceed using
396 the laboratory data as the basis for an exploration of improved models of the glacial-earthquake
397 source time function.

3 Methods

We construct synthetic seismograms using as the ‘true’ source time functions the force and pressure histories recorded in laboratory experiments and scaled up to natural glacier dimensions. We then treat these synthetic seismograms as data, and invert for glacial-earthquake source parameters using the same, CSF, approach as applied in previous studies. In these inversions we use various source time functions, $S(t)$, and evaluate the accuracy of the source parameters obtained with each type of time function.

3.1 Construction of Synthetic Seismograms

Calculation of synthetic seismograms requires the Green functions for a specified Earth structure, the amplitudes of the forces acting on the Earth at the source location, and a specified time history for those forces (Equation 1, Section 2.1). We calculate seismograms using normal-mode summation in the preliminary reference Earth model (PREM: Dziewonski & Anderson, 1981) to a minimum period of 30 s. Seismograms are calculated for a synthetic array of eleven stations located at epicentral distances between 10° and 70° from the source and equally spaced 30° apart in azimuth. The station distribution is chosen to represent the limited range of observing distances and azimuths available for analysis of glacial earthquakes at Greenland glaciers.

In this proof-of-concept study we restrict our analysis to noise-free synthetic seismograms. We anticipate the effect of noise will be small, based on the signal-to-noise ratios observed in the twenty-year glacial-earthquake catalog. In addition, Olsen and Net-

418 tles (2019) demonstrated that robust source parameters can be recovered for even very
419 small glacial earthquakes with low signal-to-noise ratios).

420 To represent the ‘true’ source time function, we use the force and pressure histo-
421 ries shown in Figure 5, recorded during experiments with analog icebergs having along-
422 flow-width vs. height aspect ratios of 0.22, 0.28, 0.43, and 0.54, similar to the range of
423 aspect ratios observed in the field for capsizing icebergs (Amundson et al., 2010). Lab-
424 oratory force and pressure histories were scaled up to field dimensions (Burton et al., 2012;
425 Murray, Nettles, et al., 2015) for iceberg heights ranging from 741-1000 m, cross-glacier
426 lengths ranging from 2360-3000 m, and along-glacier widths ranging from 160-430 m, con-
427 sistent with observed dimensions of icebergs from Jakobshavn Isbræ and Helheim Glacier
428 (e.g., Murray, Selmes, et al., 2015; James et al., 2014; Walter et al., 2012). Two to four
429 different iceberg sizes are considered for each aspect ratio.

430 We smooth the scaled-up force and pressure data using a 5-s moving average to re-
431 move high-frequency instrument noise associated with the laboratory recordings, and re-
432 move the non-zero mean background signal using 350 s of each record before signal on-
433 set. To convert pressure records to vertical-force values we multiply each pressure time
434 series by the basal area of the unrotated iceberg used for each experiment, following Murray,
435 Nettles, et al. (2015). This conversion represents a simplification compared to the true
436 ice-water-rock system, but produces a ratio of vertical to horizontal forces similar to that
437 observed for natural glacial earthquakes. In all experiments, $t = 0$ is defined as the time
438 at which the capsizing iceberg first reaches horizontal. To generate each seismic source
439 we trim the records to begin at $t = -600$ s, which is the approximate time at which the

440 signal first deviates from zero. Following iceberg capsize, water waves oscillate in the tank
441 and dominate both force and pressure records to an extent not expected in the field due
442 to damping from ice mélange (e.g., Amundson et al., 2010). We truncate the right-hand
443 side of each record at $t = +50$ s, which allows us to include source signal consistent in
444 character across experiments, while omitting the majority of later water-driven oscilla-
445 tions.

446 We parameterize the shape of each horizontal and vertical input force independently
447 using a set of isosceles triangles with durations of 10 s, fixed to overlap one another by
448 50%, to produce an accurate representation of the time series. We specify an initial west-
449 ward orientation for all horizontal forces, and an initial upwards orientation for all ver-
450 tical forces, an arbitrary choice that simplifies bookkeeping. The horizontal along-glacier
451 and vertical force functions are included as the terms $S_i(t)$ in the ground-motion equa-
452 tion; the horizontal cross-glacier term is identically zero.

453 3.2 Inversion Procedure

454 We bandpass filter the synthetic seismograms calculated in Section 3.1, transformed
455 to ground velocity, to the period band 50-150 s, consistent with standard analysis of glacial
456 earthquakes. We invert each set of input seismograms using the analysis approach em-
457 ployed in previous glacial-earthquake studies (e.g., Ekström et al., 2003; Tsai & Ekström,
458 2007; Veitch & Nettles, 2012; Olsen & Nettles, 2017), with the exception that we spec-
459 ify a wide variety of time functions $S(t)$ in our inversions, rather than using only the 50-s

460 boxcar employed in previous studies. That is, for each synthetic glacial earthquake, we
461 perform multiple inversions, each with a different specified time function $S(t)$.

462 For most experiments, wave propagation is calculated using PREM (Dziewonski
463 & Anderson, 1981), the same Earth model used to calculate the synthetic ‘data’ seismo-
464 grams, a strategy that allows us to isolate the effects of the source time function on re-
465 covery of earthquake parameters. However, the Earth’s three-dimensional seismic veloc-
466 ity structure is not perfectly known, and, in inversions of natural earthquake data, some
467 misfit to the seismograms will result from differences between the true Earth structure
468 and that specified for calculations of model seismograms. We therefore also perform some
469 experiments, using a standard 50-s boxcar time function, in which the Earth model for
470 inversion is described by the phase-velocity maps of Ekström (2011). The difference be-
471 tween the true structure in this case (PREM) and that used for inversion (the laterally
472 varying phase-velocity maps) is far greater than that expected between the real Earth
473 and high-quality models of Earth structure like those used in previous CSF inversions
474 of glacial earthquakes (e.g., Olsen & Nettles, 2017), and our experiment thus represents
475 an upper bound on the effect of mismodeled Earth structure.

476 Inversion outputs in all cases are assessed using standard criteria including the fit
477 to the data, inversion stability, and time and location shift (Ekström et al., 2012), as well
478 as recovery of the input parameters.

3.3 Construction of Model Source Time Functions

As an alternative to the 50-s boxcar time function used previously, we construct a set of models representing the earthquake force history with varying degrees of complexity. The simplest models retain the boxcar shape (Figure 4a), with a force history that integrates to zero, but we specify a variety of source durations ranging from 10–400 s.

We construct a second set of models using simplified representations of the shape of the force histories recorded in the laboratory experiments. Because GPS observations, laboratory observations, and numerical-modeling results are in general agreement on the shape and duration of the left-hand side of the glacial-earthquake source, we construct the left-hand side of most of these models from the average shape of this part of the tank experiments: We normalize the horizontal force histories recorded in eight of the tank experiments (two for each of the four aspect ratios considered), align them on the first zero-crossing time of the force history (approximately $t = -20$ s), and calculate the mean of the time series.

A second robust feature observed in all three non-seismic datasets is the rapid force reversal from up- to down-glacier orientation. Because seismic waves are efficiently generated by rapid force changes, we expect this feature may control most of the seismic signal recorded for glacial earthquakes. We therefore include a rapid force reversal in the majority of models tested in this study.

Additionally, GPS observations and laboratory results show vertical force histories with shapes generally similar to the horizontal force histories up to the time of the

500 rapid force reversal (Murray, Nettles, et al., 2015). We therefore simplify construction
501 of models in this study by specifying vertical and horizontal force functions that have
502 the same shape. That is, $S_i(t) = S(t)$ for all force components.

503 From the large suite of models we construct, we choose three representative mod-
504 els to discuss in detail (Figure 6). We refer to these as Models A, B, and C. The left-
505 hand side of Model A is constructed using the tank-average shape described above. The
506 right-hand side of Model A is constructed to include the rapid force reversal and ~ 20 s
507 of the down-glacier force taken from the tank-averaged time series. Model A does not
508 integrate to zero (Figure 6). The left-hand side of Model B is constructed using the tank-
509 average shape, and the right-hand-side is constructed as a triangle with area equal to
510 that of the left-hand side. The maximum force on the right-hand side of Model B is one
511 half the value of the maximum force on the left-hand side (Figure 6), similar in ampli-
512 tude to that observed in tank experiments 1 and 2 (Figure 5). Model C is constructed
513 in the same way as Model B, but the right-hand-side triangle has a maximum-force am-
514 plitude twice that of the maximum-force amplitude on the left-hand side (Figure 6), sim-
515 ilar to the amplitudes observed in tank experiments 7–10 (Figure 5). Models B and C
516 integrate to zero.

517 **3.4 Analysis of Inversion Results**

518 In addition to assessing how well the input location, time, and geometry of the true
519 source are recovered in our inversions, we evaluate several measures of earthquake size
520 for each event. Because the tank-derived force histories we use to generate the synthetic

521 seismograms do not integrate to zero, the input twice-integrated force history does not
522 reach a constant value (Figure 4), and a zero-frequency M_{CSF} value is not well defined.
523 The non-zero integral of the force history indicates that momentum is not conserved in
524 this simplified system. As noted earlier (Section 2.2.3), the laboratory force measure-
525 ments are made on the calving face; momentum must be transferred to other parts of
526 the tank setup, in the same way that momentum is expected to transfer to other parts
527 of the fjord in a natural glacier setting.

528 We choose to evaluate the tank-derived impulse function (Figure 4e) and the twice-
529 integrated source time function (Figure 4f) at the same point in time, when the horizon-
530 tal force first crosses zero and when the impulse function reaches its maximum value (Fig-
531 ure 4d). We refer to the value of the twice-integrated force function reported at the time
532 of maximum impulse (Figure 4f) as M_{CSF}^* to distinguish it from the zero-frequency M_{CSF}
533 value illustrated in Figure 4c. We also consider a third metric for glacial-earthquake size,
534 maximum force, defined as the maximum absolute value of the force history (e.g., Fig-
535 ure 4d). For some tank experiments, this value occurs at point (a), on the left-hand side
536 of the force history, while for others it occurs at point (b), on the right-hand side (Fig-
537 ure 5).

538 4 Results

539 Results from our inversions of seismograms calculated using the force and pressure
540 histories of Figure 5 show that earthquake locations and force azimuths are very well re-
541 covered using all source models tested, while recovery of force amplitude and other earthquake-

542 size metrics depends strongly on the source model specified, as described further below
543 and illustrated in Figures 7 – 9.

544 The majority of event latitudes (98%) are recovered to within 2.5 km, and all lon-
545 gitudes to within 6 km, regardless of the selected source model. This range of recovered
546 location values is well within the location uncertainty typical for glacial earthquakes an-
547 alyzed using the traditional boxcar-model approach (15–30 km; Veitch & Nettles, 2012).
548 Recovered force azimuths never deviate from the input values by more than 1°.

549 The orientation of the applied force with respect to horizontal, or plunge, of the
550 input model varies with time, while the inversion procedure produces a single estimate
551 of the plunge because the specified shape of the source time function $S(t)$ is the same
552 in the vertical and horizontal directions. However, the shallow plunge values recovered
553 using all models in this study (0–36°) are consistent with plunge values (3–35°) for the
554 left-hand side of the input force histories, as well as with the plunge values reported in
555 the glacial-earthquake catalog (Olsen & Nettles, 2017; Tsai & Ekström, 2007; Veitch &
556 Nettles, 2012).

557 The dependence of the recovery on input force amplitudes on the source model is
558 illustrated in Figure 7. Inversions conducted using a 50-s boxcar-shaped source model
559 (Figure 4a) return maximum-force values between 0.25 and 0.33 of the true maximum-
560 force values of the input source (Figure 7a). The corresponding maximum impulse and
561 twice-integrated force history values for the boxcar model (Figure 7b, 7c) are ~0.05–0.01
562 those of the true values, primarily because the duration of this model is less than 10%
563 that of the input source. The 50-s boxcar model produces very good fits to the tank-derived

564 waveforms, with residual variance (“misfit”) values of 0.1–0.2 (Figure 7d). We also ex-
565 periment with boxcar-shaped source models with durations ranging from 10–400 s (not
566 shown). Boxcar models with durations longer than 50 s generally recover maximum-force,
567 maximum-impulse, and twice-integrated force history values somewhat better than the
568 50-s model, but fit the input seismograms less well. The 400-s model provides the best
569 recovery of maximum force (0.3–0.4 of the true values), maximum impulse (0.3–0.9 of
570 the true values), and M_{CSF}^* values (0.5–1.3 of true values) of the boxcar models we test,
571 but produces misfit values as high as 0.5.

572 Inversions conducted using Models A, B, and C recover maximum-force values bet-
573 ter than any of the boxcar sources, including the standard 50-s boxcar (Figure 7a). Model
574 C produces maximum-force values closest to input values: 0.9–1.2 of the true values. Model
575 A also performs very well, producing maximum-force values 0.7–1 of the true values. Model
576 B performs less well, producing maximum-force values 0.6–0.9 of the true values. The
577 recovery of maximum-impulse values is dependent on iceberg aspect ratio for all three
578 models (Figure 7b). For experiments using icebergs with aspect ratios of 0.22 or 0.28 (Ex-
579 periments 1–6), Models C and A produce maximum-impulse values 0.5–0.7 of the true
580 values; Model B produces maximum-impulse values 0.7–0.9 of the true values. For ex-
581 periments using icebergs with larger aspect ratios of 0.43 or 0.54 (Experiments 7–10),
582 Models C and A recover maximum-impulse values that are 1.0 to 1.3 of the true maximum-
583 impulse values; and Model B recovers 1.4 to 1.7 of the true values. The recovery of M_{CSF}^*
584 values also depends on iceberg aspect ratio, with values underpredicted for the smaller
585 (0.22, 0.28) aspect ratios and overpredicted for the larger aspect ratios (0.43, 0.54) for

586 both models A and C (Figure 7c). Inversions using Model B produce M_{CSF}^* values that
587 exceed the true values (1.95 to 4.47) for all ten experiments.

588 Inversions using Models A and C result in low misfit values, with model seismo-
589 grams that fit the input seismograms well. Experiments using Model A produce misfit
590 values ranging from 0.05-0.25, with an average value of 0.15 (Figure 7d). Experiments
591 using Model C produce misfit values ranging from 0.06-0.32, with an average of 0.17. For
592 both Model A and Model C, the fit to the data achieved is comparable to that for the
593 50-s boxcar model. Waveforms generated using Model B are dominated by longer pe-
594 riods than the input seismograms, and fit the data less well, with misfit values ranging
595 from 0.44–0.76.

596 Results for experiments using time functions with shapes similar to Models A–C
597 but with a range of durations (from 20-1500 s) produce results consistent with those from
598 Models A–C. Event locations and force orientations are recovered very robustly, and re-
599 covery of maximum-force, maximum-impulse, and M_{CSF} values follows the behavior il-
600 lustrated in Figure 7 and described above.

601 The recovery of source parameters is only minorly affected by the use of different
602 Earth models for generation of input seismograms (PREM) and for inverse waveform mod-
603 eling (GDM52; (Ekström, 2011)). Although the imperfect representation of Earth struc-
604 ture resulting from the difference in the two Earth models produces systematic biases
605 in predicted surface-wave phase – larger than those expected for any reasonable level of
606 Earth noise – recovery of earthquake geometry and size is degraded little. In these ex-
607 periments, in which a 50-s boxcar function is used both as the true source model and

608 as the function $S(t)$ for inversion, azimuth values are recovered to within 3° and plunge
609 values to within $\sim 5^\circ$.

610 5 Discussion

611 Our experiments with synthetic glacial-earthquake data show excellent recovery of
612 earthquake geometry and location using the CSF approach, with all of the source-history
613 models we test: the 50-s boxcar; models A, B, and C; and variations on these models with
614 longer and shorter durations and different ratios of force amplitudes between the left-
615 and right-hand sides of the force history. As anticipated, results from the 50-s-boxcar
616 model underestimate the amplitude of the source. Despite the fact that the best-performing
617 models, A and C, are highly simplified compared to the true, input, force histories, and
618 do not include the variability in time-function shape observed in association with dif-
619 ferences in iceberg aspect ratio or mass, use of these models in the CSF inversion greatly
620 improves estimates of seismic amplitude. Model C appears to be the best choice among
621 the models tested, producing low misfit values and leading to robust recovery of input
622 maximum-force values.

623 In this section, we consider which source-model features are most important in pro-
624 ducing reliable inversion results, and evaluate requirements for further improvement, in-
625 cluding for top-out iceberg-calving events. We discuss the path forward for obtaining im-
626 proved source parameters for glacial earthquakes in a routine and systematic fashion,
627 and test the use of Model C on real data. We also discuss implications for interpreta-

628 tion of existing results in the published glacial-earthquake catalog, which were derived
629 using the 50-s-boxcar model.

630 **5.1 Key Components of an Improved Seismic-Source Model**

631 Our goal is a simple yet useful representation of the glacial-earthquake source, and
632 we therefore consider which features control how well source parameters are recovered.
633 Given the long (100s of seconds) force histories of the laboratory, field, and numerical
634 constraints, it is surprising that the 50-s boxcar model recovers source parameters as well
635 as it does, despite having a duration $<10\%$ that of the synthetic sources we test, and a
636 symmetric shape. It is likely that the boxcar model works well because it contains a rapid
637 force reversal that is similar to that contained in all of the input synthetic sources. This
638 rapid change in force dominates the seismic-wave excitation, and its inclusion in the source
639 model leads to better fits to the data. The rapid change in force also controls estimates
640 of earthquake timing. In all cases we test, the earthquake time estimate from CSF in-
641 version (the centroid time) produces alignment of the simplified model time function with
642 the rapid force reversal in the true source history, rather than, for example, alignment
643 between the peak force values in the true and model force histories (Figure 8).

644 Models A, B, and C also contain rapid force reversals, and recover source param-
645 eters well; Model B, which has a peak-to-peak force-reversal amplitude that is half that
646 of Model C over the same interval (Figure 8), fits the data worse than Models A and C.
647 We test an additional 16 models to investigate the effect of model shape on input-value
648 recovery, and find that models that lack a steep force reversal and instead reverse the

649 force orientation over a longer time interval have higher misfits and poorer recovery of
650 input parameters. For example, a sine-wave model with a period of 200 s returns syn-
651 thetic seismograms that fit the input data poorly, producing misfit values around 0.9,
652 and recovers maximum-force values poorly. All models we construct with a rapid force
653 reversal recover input parameters more accurately than models with more gradual force
654 reversals.

655 In addition to the rapid force reversal, the shapes of the left- and right-hand sides
656 of the models play a role in the recovery of input parameters. We test simple models that
657 approximate the general shape of Model C, but with the left-hand, tank-average shape
658 replaced by a right triangle, and the right-hand side represented by an opposing right
659 triangle of equal area. Despite capturing the rapid force reversal, these symmetric mod-
660 els do a poorer job recovering input parameters than Models A–C. Asymmetric mod-
661 els using a right triangle for the left-hand side do a similar job recovering input param-
662 eters to models constructed using tank-experiment constraints for the left-hand side (such
663 as Models A–C), and might provide a good basis for future approaches allowing scaling
664 of the time function by initial estimates of earthquake size or other parameters.

665 Models with low amplitudes of the right-hand side compared to the left-hand side
666 (like Model B) do not recover maximum force or M_{CSF} values as well as Models A or
667 C. Models with right-hand-side durations equal to or greater than the left-hand side, such
668 as Model B (Figure 6), also result in poor fits to the data. We also find very poor fits
669 to the seismograms using models that entirely omit the right-hand side, such as a model
670 constructed using the tank-average left-hand-side but stopping at the first zero cross-

671 ing of the force. This result suggests that the force history beyond the first zero cross-
672 ing plays an important role in seismic-signal generation in the frequency band of inter-
673 est. As expected, a more complicated model that mimics the complexity of the input force
674 and includes multiple zero crossings, such as that illustrated in Figure 4d, recovers in-
675 put force values well. However, because we do not yet have a full understanding of the
676 source of the force oscillations that follow the primary force reversal, and because of the
677 variability of this part of the signal between tank experiments, we limit further consid-
678 eration to models containing a single force reversal and simple shapes. Model C, which
679 captures the high-amplitude force reversal observed in the tank experiments and has a
680 right-hand duration of 200 s, provides the best fit to data of the ~ 20 models we test.

681 Our finding that the use of time functions like Models A and C leads to significantly
682 better recovery of seismic magnitude values than the boxcar model, despite the fact that
683 waveform fits are comparable between the two types of models, highlights a limitation
684 of the long-period seismic data. These data are insufficiently sensitive to the shape of
685 the source time function to discriminate one source time function from another based
686 on waveform fits alone, as previously recognized by Tsai and Ekström (2007) and Tsai
687 et al. (2008), as long as the source shapes in question include the key characteristics de-
688 scribed here. However, our results demonstrate that including knowledge of the source
689 shape derived from other datasets can markedly improve recovery of glacial-earthquake
690 size.

5.2 Limitations on Direct Inversion for Force History

An open question remains whether more flexibility in the CSF inversion could be provided, within the limits of waveform sensitivity, by inverting for the source time function along with other parameters, with the time function parameterized by a small number of simple shapes. This approach has been used successfully to obtain more detailed source histories for landslides (e.g., Ekström & Stark, 2013). We experiment with using the Landslide-Force-History (LFH) technique (Ekström & Stark, 2013) to invert directly for the shape of the glacial-earthquake force function. In these inversions we restrict the force function to consist of a small number (4-8) of isosceles triangles overlapping by 50%. We solve for the amplitude of each triangular sub-source, and allow horizontal and vertical forces to vary independently. To minimize oscillation in the force functions we apply a weak smoothing constraint to these models. The force histories are constrained to integrate to zero.

We find that a simple 50-s LFH model with four sub-sources overlapping by 50% reproduces the input force to within 50% (Figure 7a). Misfits for these experiments are higher than those using a boxcar model, but are within the range found for published glacial earthquakes. Extending the duration of the four sub-sources to 40 s, resulting in a full source duration of 100 s, produces maximum-force values similar to results using a 50-s LFH model, and similar fits to data. Though all evidence points to a source time function that is significantly longer than 100 s, experiments that further lengthen the duration of each sub-source lead to poor parameter recovery and high misfits. This is likely due to the fact that a rapid force reversal is not captured by an LFH source when

713 long-duration sub-sources (≥ 50 s) are used. We also experiment with increasing the num-
714 ber of shorter-duration (10–20 s) sub-sources as an alternative way to increase the full
715 source duration. However, larger numbers of sub-sources lead to force histories that con-
716 tain multiple rapid force oscillations that are inconsistent with our knowledge of the left-
717 hand side of the source, even with the damping constraint. In addition, these experiments
718 frequently return down-glacier force orientations, 180° from the input orientation.

719 Applying the LFH approach to real glacial-earthquake data produces similarly un-
720 satisfactory results. For ten glacial earthquakes that occurred at Helheim Glacier and
721 Jakobshavn Isbræ, we find high misfit values (0.4–0.8) using the model with 40 s sub-
722 source duration, and force histories that oscillate in what we believe to be a non-physical
723 way for many of the glacial earthquakes using the 70- and 80-s models, similar to the be-
724 havior we observe in the experiments using synthetic seismograms. As for the experi-
725 ments with fixed source shapes, we conclude that the available seismic data are, in gen-
726 eral, not sufficient to constrain the shape of the glacial-earthquake source time function
727 on their own. While the LFH-modeling technique has proven successful with landslide
728 data (Ekström & Stark, 2013), glacial-earthquake data constraints are poorer, owing in
729 part to longer source-to-station distances for glacial earthquakes and poorer azimuthal
730 station coverage.

731 Sergeant et al. (2016) also investigated the possibility of solving directly for the force
732 history of a glacial earthquake, using a deconvolution technique to estimate the source
733 time function from displacement seismograms. However, the force histories they recover
734 also contain rapid oscillations in both the horizontal and vertical forces that are not ob-

735 served in any of the independent constraints from laboratory or field observations, and
736 Sergeant et al. (2016) note that the rapid force oscillations have no physical basis.

737 While ideally we could obtain a description of the full force history directly from
738 the seismic data, neither the LFH approach nor the approach of Sergeant et al. (2016)
739 produces satisfactory results. The natural depletion of the glacial-earthquake seismograms
740 in short-period energy, combined with sparse station coverage, make routine, indepen-
741 dent estimation of the source time function infeasible at this time. The use of a fixed,
742 but physically informed, time function is thus our preferred path forward for improving
743 glacial-earthquake source-parameter estimates.

744 **5.3 Maximum Force as a Preferred Metric of Glacial-Earthquake Size**

745 The M_{CSF} value has been used in most studies of glacial earthquakes to date, in-
746 cluding by the current authors, to provide a summary measure of earthquake size. The
747 quantity was originally defined by Kawakatsu (1989) in an application of CSF inversion
748 to landslides. As shown in Figure 4, it represents the integral of the momentum of the
749 landslide mass or accelerating iceberg, with the static M_{CSF} value taken once the ac-
750 celeration is complete (Figure 4c). In this sense, M_{CSF} is analogous to the seismic scalar
751 moment M_0 , which is the preferred summary measure of size for tectonic earthquakes
752 and represents the seismic moment after fault slip is complete. Although the M_{CSF} value
753 is well defined when the force history integrates to zero (e.g., Figure 4a, b, c), and mo-
754 mentum is conserved within the limited region of the iceberg and calving front, it is clear
755 from the tank data, GPS data, and numerical models that the momentum budget is not

756 closed within this limited system. The momentum transfer that must occur to other parts
757 of the Earth system does not appear to generate significant seismic energy, and, at this
758 time, our knowledge of that longer-timescale component of the momentum budget is too
759 limited to include in the source model for the glacial earthquakes.

760 As long as the true duration and shape of the glacial-earthquake source time func-
761 tion are unknown, serious limitations exist in the use of the M_{CSF} metric and its inter-
762 pretation, primarily because values of M_{CSF} estimated from seismic data are highly sen-
763 sitive to the shape and duration of the specified force-time function. However, our ex-
764 periments show that the value of the maximum force acting during a glacial earthquake
765 can be recovered robustly, and is far less sensitive to assumptions about the force-time
766 history than is the M_{CSF} value (Figure 7). The maximum-force values (Figure 7a) are
767 better recovered than are M_{CSF} values (Figure 7c) for both the traditional boxcar model
768 and for our preferred model, Model C, for example. Furthermore, maximum-force val-
769 ues are recovered well across the full range of aspect ratios we test (Figure 7a; aspect
770 ratio for each experiment given in Figure 5), whereas recovery of M_{CSF}^* values is notably
771 poorer in experiments with higher iceberg aspect ratios (experiments 7–10, Figure 7c).
772 We therefore suggest that, at this time, the maximum force provides a better, simple mea-
773 sure of glacial-earthquake size than the M_{CSF} value that has been reported to date in
774 the glacial-earthquake literature (Olsen & Nettles, 2017, 2019; Tsai & Ekström, 2007;
775 Veitch & Nettles, 2012). We note that Sergeant et al. (2019) also considered the max-
776 imum force generated during a rotational calving event, and discussed advantages to this
777 size metric as opposed to M_{CSF} .

5.4 Relationship between Maximum Force and Iceberg Mass

For the tank experiments, the iceberg mass correlates with all three measures of glacial-earthquake size we consider: maximum force, maximum impulse, and M_{CSF}^* , where these values are read from the recorded force histories (grey squares in Figure 9). The dominant relationship in all cases is an increase in the seismic-magnitude parameters with increasing iceberg size. Analog icebergs with aspect ratios of 0.22 and 0.28 demonstrate a slightly different trend than those with aspect ratios of 0.43 and 0.54 (Figure 9a), owing to the higher peak amplitudes of the down-glacier force recorded in experiments of larger aspect ratio, compared with those of smaller aspect ratio (Figure 5).

Like the direct observations of force from the tank experiments, the seismic-magnitude values recovered using all five of the models discussed in detail in this study correlate positively with iceberg mass (Figure 9). Models A, B, and C do a better job capturing the relationship between iceberg mass and maximum force than does the boxcar model (Figure 9a). Despite the simplicity of Models A, B, and C, they each capture the difference in trend between larger and smaller aspect ratios that the tank observations display. In particular, maximum-force values recovered using Model C match the trend of the tank observations well for both small and large aspect ratios, and recover maximum-force values very close to the tank values (Figure 9a).

Improved recovery of all three seismic-magnitude metrics using Models A and C (Figures 7, 9) is encouraging, and suggests the potential utility of reanalyzing real glacial-earthquake data using a more-sophisticated model. We use Model C in an analysis of twelve glacial earthquakes previously studied using the 50-s boxcar model (circles and

800 squares in Figure 2) to test the approach. We find that maximum-force values are posi-
801 tively correlated with iceberg mass (yellow diamonds, Figure 10), as they are for the re-
802 sults with the boxcar model (black dots in Figure 10). As expected from our synthetic
803 experiments, maximum-force values recovered using Model C are higher than those cal-
804 culated for the same events using the boxcar model. The values for the real earthquakes
805 obtained using Model C occupy approximately the same space in the maximum-force vs.
806 mass diagram as the values from the scaled-up tank experiments (Figure 10), suggest-
807 ing that the values are likely to be realistic.

808 Sergeant et al. (2019) use a different approach to investigate the relationship be-
809 tween seismic magnitude and iceberg size. They estimate force histories using a decon-
810 volution technique, and compare these histories to bandpass-filtered, numerically mod-
811 eled force histories for capsizes of a range of iceberg sizes. By performing a grid search
812 over possible modeled force histories, they identify the height and iceberg aspect ratio
813 of the model that most closely fits the data. They then consider a range of plausible ice-
814 berg cross-flow-length values and calculate an average volume estimate for a single ice-
815 berg. The iceberg volumes estimated using this technique come from model results, with
816 limitations discussed earlier, and are not constructed by independent observations of ice-
817 berg size. Whereas we observe only a minor dependence of seismic-magnitude param-
818 eters on iceberg aspect ratio, a clear aspect-ratio dependence is observed in the relation-
819 ship reported by Sergeant et al. (2019) between maximum force and model predictions
820 of iceberg size. We discuss the need for further exploration of aspect-ratio dependence
821 in Section 5.7.

5.5 The Boxcar Model and Implications for Published Results

All evidence points to a true glacial-earthquake source duration longer than 50 s, which means that the M_{CSF} values reported in the glacial-earthquake literature almost certainly underestimate true M_{CSF} values, possibly by more than an order of magnitude. However, this underprediction appears to depend little on iceberg aspect ratio or mass, explaining the good observed correlation between iceberg size and M_{CSF} (Figure 2) and results using the more sophisticated source models evaluated here (Figures 9 and 10). Maximum-force values can be calculated from the M_{CSF} values estimated in previous studies using a boxcar-shaped model (Olsen & Nettles, 2017, 2019; Tsai & Ekström, 2007; Veitch & Nettles, 2012) in a straightforward manner. For a boxcar model like that shown in Figure 4a, $M_{CSF} = F_{max} \cdot (T_H)^2$, where T_H is the half duration of the force function, or 25 s for a 50-s boxcar model. Our results suggest that multiplication of these maximum-force values by a factor of 3–4 would bring them close to the likely true values (Figure 7a).

5.6 Top-Out Calving Events

As noted earlier, top-out calving events, in which the top surface of the iceberg rotates outward towards the fjord and the bottom of the berg rotates towards the calving face, are believed to be rare in comparison with bottom-out calving events. However, some such events are known to occur, and data are available from one analog experiment of top-out iceberg calving. We therefore explore source-parameter recovery for this, single, experiment using the same approach as for the bottom-out events. In laboratory ex-

843 periments, top-out iceberg capsizes only when an initial angle of rotation for the
844 iceberg is enforced, in contrast to the spontaneous capsizing observed for bottom-out calving
845 experiments (Amundson et al., 2012; Cathles et al., 2015). The experimental setup
846 for top-out calving experiments is otherwise the same as for bottom-out experiments,
847 and we follow the same data-processing and inversion steps.

848 The horizontal force and pressure histories recorded during the top-out experiment,
849 which used an analog iceberg of aspect ratio 0.28, are shown in Figure 11a. The horizontal-
850 force time series generated by top-out calving lacks the negative-force excursion observed
851 in bottom-out experiments just after $t = 0$ s ('b' in Experiment 1, Figure 5), and the top-
852 out pressure time series is more variable in the first 500 s than in bottom-out experiments.
853 After $t = 0$ s the horizontal force and pressure histories from the top-out calving exper-
854 iment smoothly transition to in-phase oscillation similar to that observed in bottom-out
855 calving experiments.

856 As for the bottom-out experiments, waveform modeling recovers the force azimuth
857 for the top-out experiment to within less than one degree. The maximum force observed
858 in the top-out calving event is recovered better using Models A, B, and C than using the
859 50 s boxcar model, as is true for all of the bottom-out events (Figure 11b). However, the
860 maximum force recovered is underestimated using all of the models, and using our pre-
861 ferred Model C, is only 0.5 of the input-force value. The misfit to the waveforms is high
862 for all models, and for Model C is 0.6, much higher than the average misfit (0.17) for the
863 10 bottom-out calving experiments using Model C (Figure 11c).

864 As discussed in Section 2.2.1, the main glacial-earthquake signal is likely generated
865 by the rapid force reversal around $t = 0$ s observed in the ten bottom-out calving ex-
866 periments as well as in field observations from Helheim Glacier (Murray, Nettles, et al.,
867 2015). The underestimation of the maximum-force value for the top-out experiment there-
868 fore likely comes from the fact that the source models used (boxcar, A, B, C) contain
869 a deceleration phase that includes negative force values immediately following $t = 0$ s
870 (Figure 6), while the tank-recorded force history (Figure 11a) does not. This interpre-
871 tation is supported by the observation that Model B, which has the smallest negative-
872 force excursion of the models considered here (Figure 6) both does the best job recov-
873 ering the maximum-force value for the top-out experiment and has the lowest misfit (Fig-
874 ure 11c), in contrast with the results for the bottom-out events.

875 Future work on these events could investigate whether high misfit values for top-
876 out calving events might be a reliable diagnostic tool to separate top-out events and to
877 flag them for further analysis. Such an approach might then be the first step in a work-
878 flow using a separate top-out source model, optimized to work with these less-common
879 events.

880 **5.7 Future Considerations in Source-Model Development**

881 The work in this study demonstrates the feasibility of, and important improvement
882 from, incorporating physics-based information into the glacial-earthquake source model,
883 and provides a framework for future work. Further improvements to modeling of the glacial-
884 earthquake source can build upon this proof-of-concept study in two ways: 1) increas-

885 ing the sophistication of the seismic-source parameterization used in the inversion pro-
886 cedure, and 2) additional analog calving experiments to elucidate the full nature of the
887 seismic source.

888 In the current study, we maintained the requirement used in previous CSF anal-
889 yses of glacial earthquakes that the shapes of the vertical and horizontal force histories
890 be the same. Because laboratory and geodetic field data show that the shapes are in-
891 deed very similar prior to the force reversal, and because the vertical force amplitude is
892 typically less than 20% that of the horizontal, this simplifying assumption was justified
893 in our proof-of-concept study. However, future work should investigate possible improve-
894 ments from using models with different shapes for the horizontal and vertical force his-
895 tories. Constructing a model for the vertical force history using pressure records from
896 laboratory experiments, converted to vertical force, might improve source-parameter re-
897 covery: our results suggest that the iceberg deceleration phase (i.e., the right-hand side
898 of the source), may be more important to generation of the seismic signal than previ-
899 ously recognized, and it is during this time that the vertical- and horizontal-force his-
900 tories differ most in shape.

901 Future work might also explore the utility of scaling the shape or duration of the
902 force-time model based on iterative estimation of glacial-earthquake size. Such an ap-
903 proach is standard in CMT analysis of tectonic earthquakes (Ekström & Nettles, 2014),
904 and may aid in modeling of glacial earthquakes, particularly in light of the range of ice-
905 berg sizes now known to generate glacial earthquakes (Olsen & Nettles, 2019).

906 Similarly, future tank experiments designed specifically to advance understanding
907 of the glacial-earthquake source would be valuable. The role iceberg aspect ratio plays
908 in determining the shape of the force history should be explored further, with additional
909 laboratory experiments using analog icebergs with a larger range of aspect ratios. Un-
910 certainty regarding the character of the right-hand side of the seismic source is currently
911 a limitation, and obtaining data from the region of the tank away from the calving front
912 might help clarify important aspects of the source. Because no geodetic field observa-
913 tions exist of top-out calving, analog experiments offer the primary means to explore this
914 calving geometry. Additional tank experiments of top-out calving would aid exploration
915 of the variability of force and pressure histories generated by iceberg capsize with this
916 geometry (e.g., for icebergs with a range of aspect ratios), and could potentially be used
917 to develop a source model specifically for top-out calving events. Numerical modeling
918 that includes hydrodynamic forces, and the right-hand side of the force history, would
919 also be helpful; some such work is currently underway (Bonnet et al., 2020).

920 **6 Conclusions**

921 In this study we have explored the feasibility of improving estimates of glacial-earthquake
922 source parameters through incorporation of improved knowledge of the earthquake source
923 time function. In particular, we have explored the utility of replacing the boxcar-shaped
924 function used in previous work (Olsen & Nettles, 2017, 2019; Tsai & Ekström, 2007; Veitch
925 & Nettles, 2012) with a more sophisticated time function based on knowledge obtained
926 from laboratory, field, and numerical-modeling studies (Cathles et al., 2015; Murray, Net-
927 tles, et al., 2015; Sergeant et al., 2018).

928 We demonstrate that use of a source model that closely represents the true source
929 of seismic waves (as is the case in this study for Model C and the synthetic seismograms
930 we generate using tank-experiment observations), robustly retrieves source parameters
931 of a seismic event. Even without a full physical description of the glacial-earthquake source,
932 greatly improved estimates of source parameters can be obtained by this straightforward
933 extension of the centroid-single-force modeling approach. We find that the rapid rever-
934 sal in force, from upglacier to downglacier, that occurs as a calving iceberg nears hor-
935 izontal is the most important feature to include in the force-time model. This finding
936 likely explains the success of the highly simplified, boxcar, model used in earlier stud-
937 ies. Previous numerical-modeling work (Sergeant et al., 2018) focused exclusively on the
938 acceleration phase of the glacial-earthquake source; however, we find that the deceler-
939 ation phase of the source time function also plays a role in generating waveforms that
940 has not previously been appreciated.

941 The force-time model that we found to provide a good balance of simplicity and
942 effectiveness in our proof-of-concept study, ‘Model C’, captures the gradual force onset
943 observed in the acceleration phase of the laboratory experiments we investigate. It con-
944 tains the rapid force reversal from up to downglacier, and contains a ~ 200 s decelera-
945 tion phase. Model C recovers source parameters well for icebergs with a range of aspect
946 ratios, an important finding given our limited knowledge of the true aspect ratios of cap-
947 sizing icebergs. The waveform-modeling approach we apply in this study is simple, com-
948 putationally efficient, and returns robust estimates of source parameters despite the data-
949 quality limitations inherent to work with glacial earthquakes. By incorporating non-seismic

950 constraints on the shape of the force history, we overcome limitations associated with
951 the sensitivity of long-period seismic data and produce better recovery of seismic-magnitude
952 values.

953 Using synthetic seismograms, we demonstrate that the maximum force generated
954 by a calving iceberg can be more accurately retrieved than the twice-integrated force value,
955 M_{CSF} . We therefore prefer maximum force as a seismically derived measure of glacial-
956 earthquake size: it provides a simple metric that is far less sensitive to modeling choices
957 than integrated measures. We find that maximum-force values associated with M_{CSF}
958 values reported for events in the published glacial-earthquake catalog likely underpre-
959 dict true maximum-force values by a factor of 3-4 owing to the short duration and fixed
960 shape of the 50-s boxcar model used, but that the underprediction is nearly constant across
961 iceberg mass and aspect ratio, allowing for simple reconstruction of more accurate val-
962 ues.

963 The results we derive here from constructing and implementing a new generation
964 of physics-based seismic-source models are an important step towards obtaining more
965 accurate relationships between iceberg mass and seismic observables, and between phys-
966 ical quantities controlling iceberg calving dynamics. These improvements also form an
967 important step towards the use of glacial-earthquake data as a geophysical tool for mass-
968 loss estimation.

969 **Acknowledgments**

970 K.G. Olsen was supported by an NSF Graduate Research Fellowship (DGE-1644869).

971 K.G. Olsen and M. Nettles also acknowledge support from NSF grants EAR-1639131 and

972 EAR-1936254. T. Murray and T. James were supported by Natural Environment Re-

973 search Council grant NERC NE/I007148/1. J.C. Burton was supported by NSF grant

974 DMR-1506446. We appreciate constructive comments from two anonymous reviewers and

975 Editor Paul Winberry.

976 **7 Conflict of Interest**

977 The authors are not aware of any conflicts of interest relevant to this study.

978 **8 Data Availability Statement**

979 We acknowledge the use of seismic data from the Greenland Ice Sheet Monitoring

980 Network and the Global Seismographic Network. All seismic data are publicly available

981 from the IRIS DMC (<https://ds.iris.edu/ds/nodes/dmc/>). Data that underpin the fig-

982 ures in this manuscript are available in a repository on the Harvard Dataverse (doi.org/10.7910/DVN/P3Q8RA).

983 Seismic analyses were completed using the Python library ObsPy (Beyreuther et al., 2010).

984 Figures were made using the Matplotlib Python library (Hunter, 2007).

985 **References**

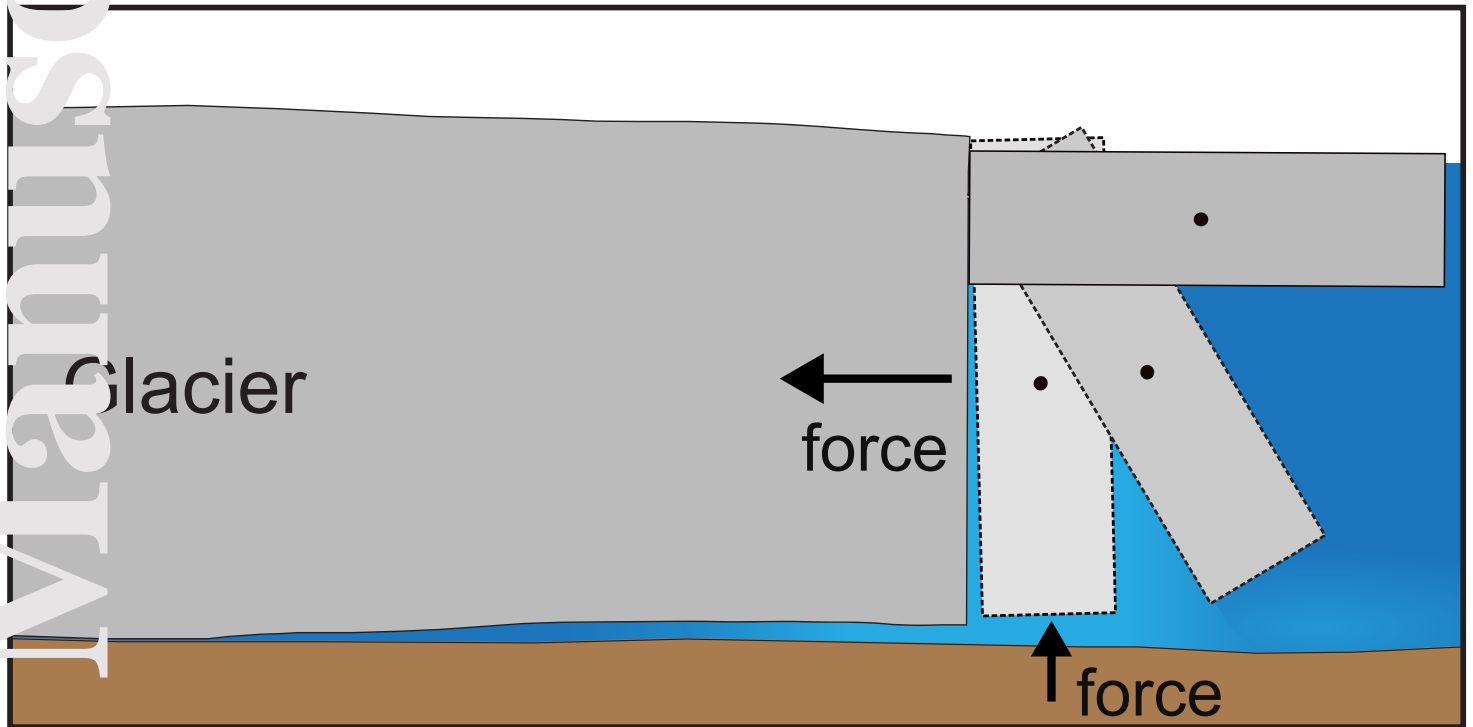
- 986 Amundson, J. M., Burton, J. C., & Correa-Legisios, S. (2012). Impact of hydrody-
 987 namics on seismic signals generated by iceberg collisions. *Annals of Glaciology*,
 988 *53*(60), 106–112. doi: 10.3189/2012/AoG60A012
- 989 Amundson, J. M., Fahnestock, M., Truffer, M., Brown, J., Lüthi, M. P., & Motyka,
 990 R. J. (2010). Ice mélange dynamics and implications for terminus stabil-
 991 ity, Jakobshavn Isbræ, Greenland. *Journal of Geophysical Research: Earth*
 992 *Surface*, *115*(F1). doi: 10.1029/2009JF001405
- 993 Beyreuther, M., Barsch, R., Krischer, L., Megies, T., Behr, Y., & Wassermann, J.
 994 (2010). Obspy: A python toolbox for seismology. *Seismological Research*
 995 *Letters*, *81*(3), 530–533. doi: 10.1785/gssrl.81.3.530
- 996 Bonnet, P., Yastrebov, V. A., Queutey, P., Leroyer, A., Mangeney, A., Castel-
 997 nau, O., ... Montagner, J.-P. (2020). Modelling capsizing icebergs in the
 998 open ocean. *Geophysical Journal International*, *223*(2), 1265–1287. doi:
 999 10.1093/gji/ggaa353
- 1000 Burton, J. C., Amundson, J. M., Abbot, D. S., Boghosian, A., Cathles, L. M.,
 1001 Correa-Legisios, S., ... MacAyeal, D. R. (2012). Laboratory investigations
 1002 of iceberg capsize dynamics, energy dissipation and tsunamigenesis. *Journal of*
 1003 *Geophysical Research: Earth Surface*, *117*(F1). doi: 10.1029/2011JF002055
- 1004 Cathles, L. M., Kaluzienski, L., & Burton, J. C. (2015, December). Laboratory in-
 1005 vestigations of seismicity caused by iceberg calving and capsize. In *AGU Fall*
 1006 *Meeting Abstracts*.

- 1007 Dziewonski, A. M., & Anderson, D. L. (1981). Preliminary reference Earth model.
1008 *Phys. Earth Planet. Inter.*, 25(4), 297–356. doi: 10.1016/0031-9201(81)90046
1009 -7
- 1010 Dziewonski, A. M., Chou, T.-A., & Woodhouse, J. H. (1981). Determination of
1011 earthquake source parameters from waveform data for studies of global and
1012 regional seismicity. *J. Geophys. Res.: Solid Earth*, 86(B4), 2825–2852.
- 1013 Ekström, G. (2011). A global model of Love and Rayleigh surface wave dispersion
1014 and anisotropy, 25-250 s. *Geophysical Journal International*, 187(3), 1668–
1015 1686. doi: 10.1111/j.1365-246X.2011.05225.x
- 1016 Ekström, G., & Nettles, M. (2014). Long-Period Moment-Tensor Inversion: The
1017 Global CMT Project. *Encyclopedia of Earthquake Engineering*, 1–13. doi: 10
1018 .1007/978-3-642-36197-5_291-1
- 1019 Ekström, G., Nettles, M., & Abers, G. A. (2003). Glacial earthquakes. *Science*,
1020 302(5645), 622–624. doi: 10.1126/science.1088057
- 1021 Ekström, G., Nettles, M., & Dziewoński, A. M. (2012). The global CMT project
1022 2004–2010: centroid-moment tensors for 13,017 earthquakes. *Phys. Earth
1023 Planet. Inter.*, 200, 1–9. doi: 10.1016/j.pepi.2012.04.002
- 1024 Ekström, G., Nettles, M., & Tsai, V. C. (2006). Seasonality and increasing frequency
1025 of Greenland glacial earthquakes. *Science*, 311(5768), 1756–1758. doi: 10
1026 .1126/science.1122112
- 1027 Ekström, G., & Stark, C. P. (2013). Simple scaling of catastrophic landslide dynam-
1028 ics. *Science*, 339(6126), 1416–1419. doi: 10.1126/science.1232887

- 1029 Enderlin, E. M., Howat, I. M., Jeong, S., Noh, M.-J., Angelen, J. H., & van den
1030 Broeke, M. R. (2014). An improved mass budget for the Greenland ice sheet.
1031 *Geophys. Res. Lett.*, *41*(3), 866–872. doi: 10.1002/2013GL059010
- 1032 Heller, V., Chen, F., Brühl, M., Gabl, R., Chen, X., Wolters, G., & Fuchs, H.
1033 (2019). Large-scale experiments into the tsunamigenic potential of different
1034 iceberg calving mechanisms. *Scientific reports*, *9*(1), 1–10. doi: 36634-3
- 1035 Hunter, J. D. (2007). Matplotlib: A 2D Graphics Environment. *Computing in Sci-*
1036 *ence & Engineering*, *9*(03), 90–95. doi: 10.1109/MCSE.2007.55
- 1037 James, T. D., Murray, T., Selmes, N., Scharrer, K., & O’Leary, M. (2014). Buoy-
1038 ant flexure and basal crevassing in dynamic mass loss at Helheim Glacier. *Nat.*
1039 *Geosci.*, *7*(8), 593–596. doi: 10.1038/NGEO2204
- 1040 Kawakatsu, H. (1989). Centroid single force inversion of seismic waves generated by
1041 landslides. *J. Geophys. Res.: Solid Earth*, *94*(B9), 12363–12374. doi: 10.1029/
1042 JB094iB09p12363
- 1043 MacAyeal, D. R., Abbot, D. S., & Sergienko, O. V. (2011). Iceberg-capsize
1044 tsunamigenesis. *Annals of Glaciology*, *52*(58), 51–56. doi: 10.3189/
1045 172756411797252103
- 1046 Moon, T., Joughin, I., Smith, B. E., & Howat, I. M. (2012). 21st-century evolution
1047 of Greenland outlet glacier velocities. *Science*, *336*(6081), 576–578. doi: 10
1048 .1126/science.1219985
- 1049 Murray, T., Nettles, M., Selmes, N., Cathles, L. M., Burton, J. C., James, T. D.,
1050 ... others (2015). Reverse glacier motion during iceberg calving and

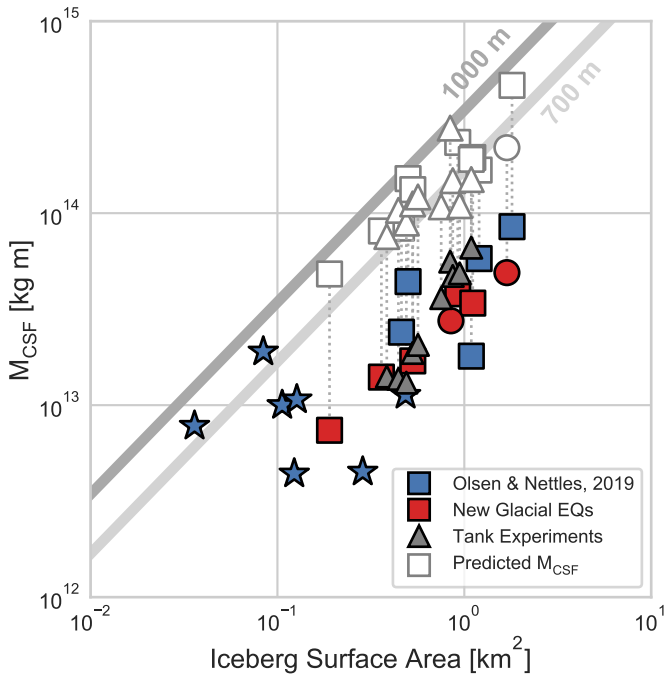
- 1051 the cause of glacial earthquakes. *Science*, *349*(6245), 305–308. doi:
1052 10.1126/science.aab0460
- 1053 Murray, T., Selmes, N., James, T. D., Edwards, S., Martin, I., O’Farrell, T., ...
1054 Baugé, T. (2015). Dynamics of glacier calving at the ungrounded margin of
1055 Helheim Glacier, southeast Greenland. *J. Geophys. Res.: Earth Surf.*, *120*(6),
1056 964–982. doi: 10.1002/2015JF003531
- 1057 Nettles, M., & Ekström, G. (2010). Glacial earthquakes in Greenland and
1058 Antarctica. *Annual Review of Earth and Planetary Sciences*, *38*. doi:
1059 10.1146/annurev-earth-040809-152414
- 1060 Nettles, M., Larsen, T. B., Elósegui, P., Hamilton, G. S., Stearns, L. A., Ahlstrøm,
1061 A. P., ... others (2008). Step-wise changes in glacier flow speed coincide with
1062 calving and glacial earthquakes at Helheim Glacier, Greenland. *Geophys. Res.*
1063 *Lett.*, *35*(24), L24503. doi: 10.1029/2008GL036127
- 1064 Olsen, K. G., & Nettles, M. (2017). Patterns in glacial-earthquake activity around
1065 Greenland, 2011–13. *Journal of Glaciology*, *63*(242), 1077–1089. doi: 10.1017/
1066 jog.2017.78
- 1067 Olsen, K. G., & Nettles, M. (2019). Constraints on terminus dynamics at Greenland
1068 glaciers from small glacial earthquakes. *Journal of Geophysical Research: Earth*
1069 *Surface*. doi: 10.1029/2019JF005054
- 1070 Sergeant, A., Mangeney, A., Stutzmann, E., Montagner, J., Walter, F., Moretti, L.,
1071 & Castelnau, O. (2016). Complex force history of a calving-generated glacial
1072 earthquake derived from broadband seismic inversion. *Geophys. Res. Lett.*,

- 1073 43(3), 2015GL066785. doi: 10.1002/2015GL066785
- 1074 Sergeant, A., Mangeney, A., Yastrebov, V. A., Walter, F., Montagner, J.-P., Castel-
1075 nau, O., ... others (2019). Monitoring Greenland ice sheet buoyancy-driven
1076 calving discharge using glacial earthquakes. *Annals of Glaciology*, 1–21. doi:
1077 10.1017/aog.2019.7
- 1078 Sergeant, A., Yastrebov, V. A., Mangeney, A., Castelnau, O., Montagner, J.-P., &
1079 Stutzmann, E. (2018). Numerical modeling of iceberg capsizing responsible for
1080 glacial earthquakes. *Journal of Geophysical Research: Earth Surface*, 123(11),
1081 3013–3033. doi: 10.1029/2018JF004768
- 1082 Tsai, V. C., & Ekström, G. (2007). Analysis of glacial earthquakes. *J. Geophys.*
1083 *Res.: Earth Surf.*, 112(F3), F03S22. doi: 10.1029/2006JF000596
- 1084 Tsai, V. C., Rice, J. R., & Fahnestock, M. (2008). Possible mechanisms for glacial
1085 earthquakes. *Journal of Geophysical Research: Earth Surface*, 113(F3). doi: 10
1086 .1029/2007JF000944
- 1087 Veitch, S. A., & Nettles, M. (2012). Spatial and temporal variations in Greenland
1088 glacial-earthquake activity, 1993–2010. *J. Geophys. Res.: Earth Surf.*, 117(F4),
1089 ISSN 2156-2202. doi: 10.1029/2012JF002412
- 1090 Walter, F., Amundson, J. M., O’Neel, S., Truffer, M., Fahnestock, M., & Fricker,
1091 H. A. (2012). Analysis of low-frequency seismic signals generated during a
1092 multiple-iceberg calving event at Jakobshavn Isbræ, Greenland. *J. Geophys.*
1093 *Res.: Earth Surf.*, 117(F1), F01036. doi: 10.1029/2011JF002132

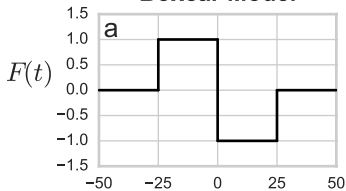


This is the author manuscript accepted for publication and has undergone full peer review but has not been through the copyediting, typesetting, pagination and proofreading process, which may lead to differences between this version and the [Version of Record](#). Please cite this article as doi: [10.1029/2021JF006384](https://doi.org/10.1029/2021JF006384).

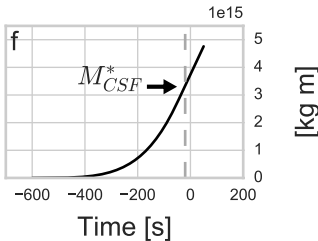
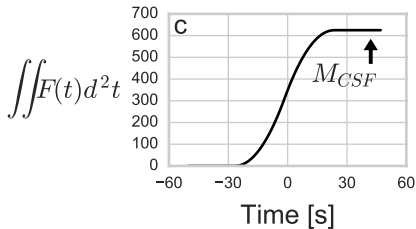
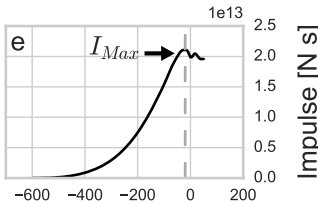
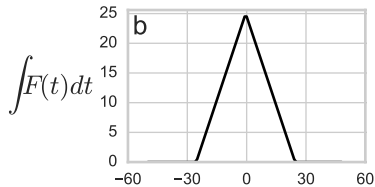
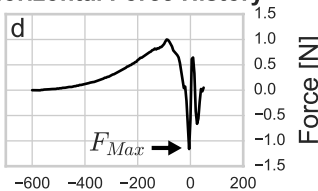
This article is protected by copyright. All rights reserved.



Boxcar Model



Tank-Derived Horizontal Force History



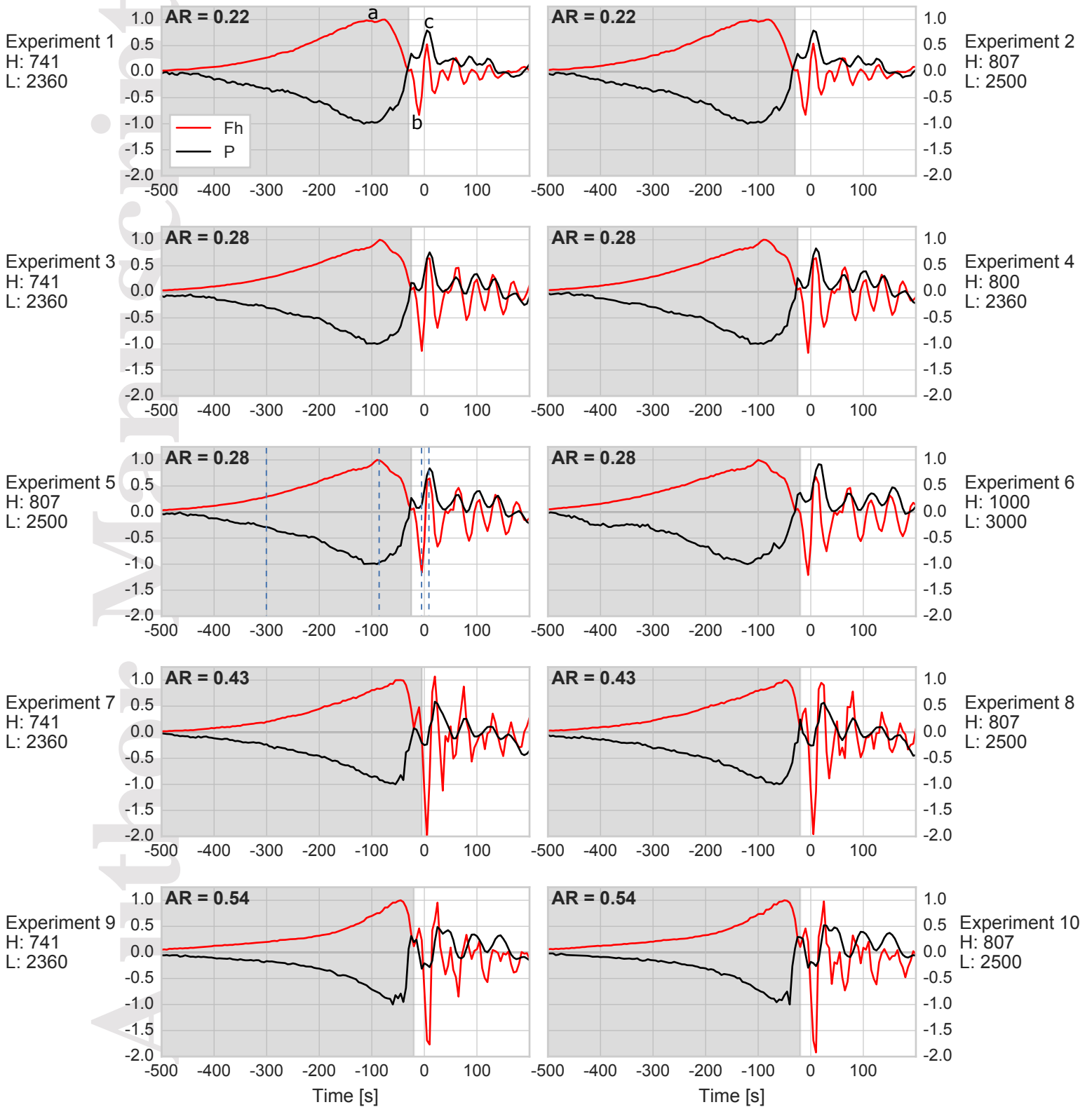
Instrumented
Terminus

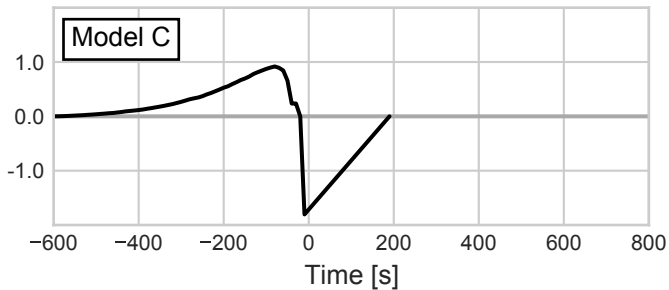
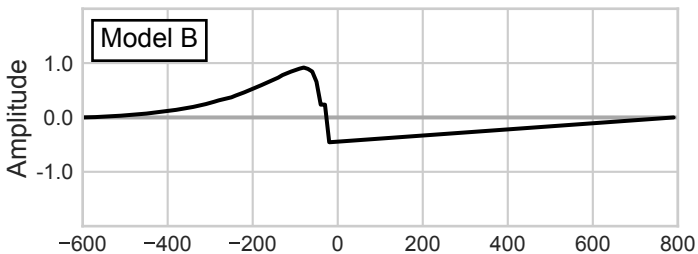
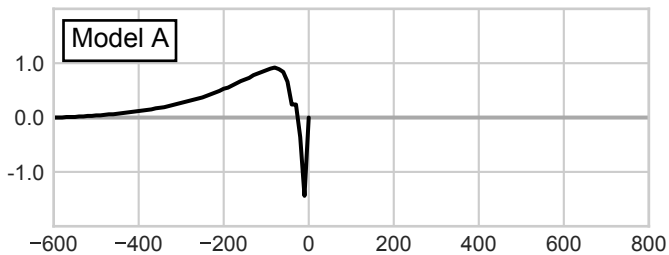
-300 s

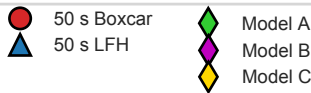
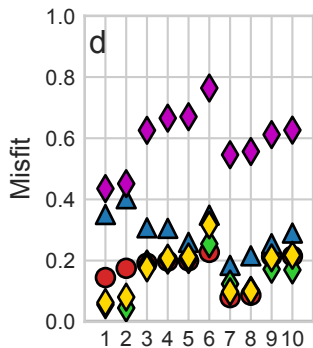
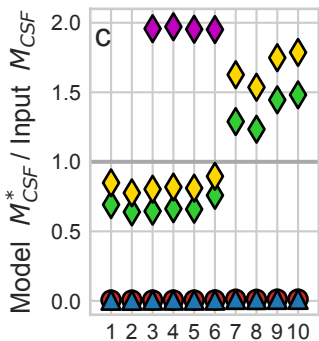
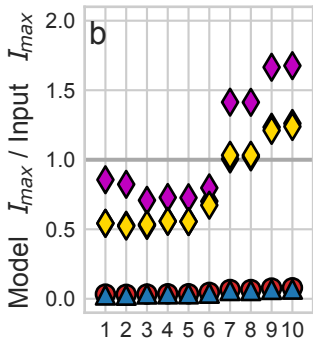
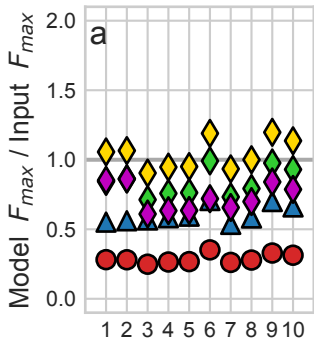
-85 s

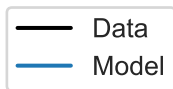
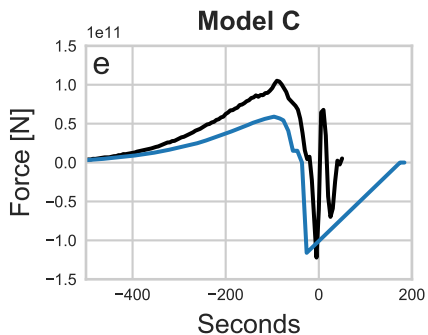
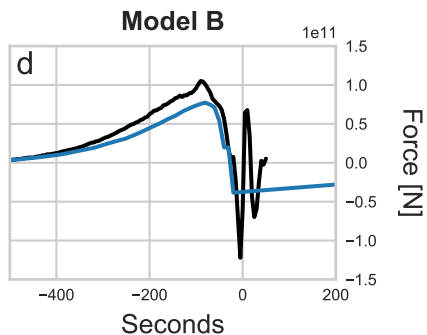
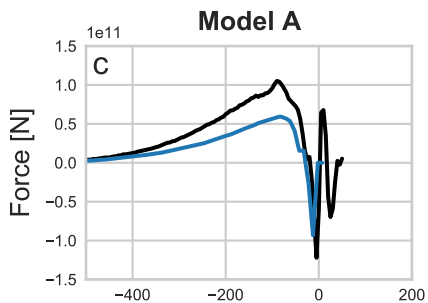
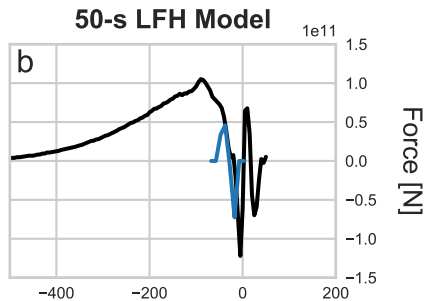
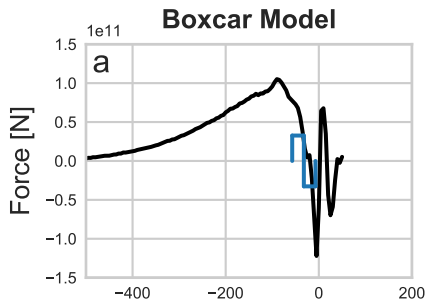
-5 s

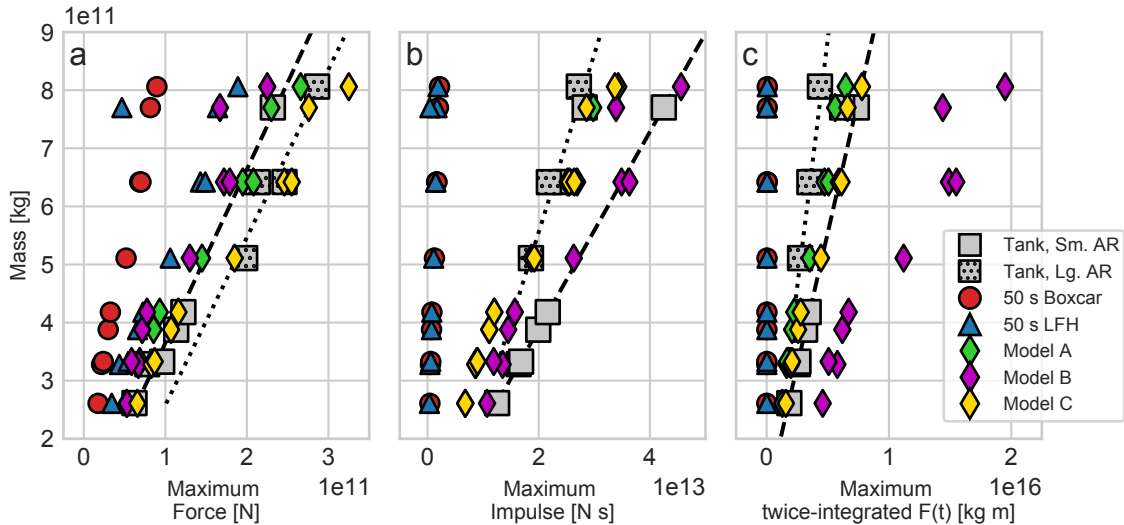
+8 s

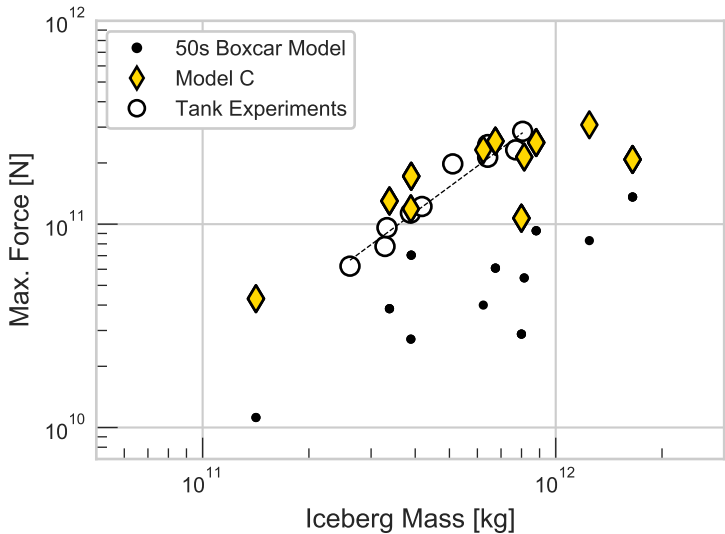












Experiment 11
H: 1000
L: 3000
AR: 0.28

